Daytime and nighttime aerosol soluble iron formation in clean and slightly-polluted moisture air in a coastal city in eastern China

Wenshuai Li[1,2], Yuxuan Qi[1,2], Yingchen Liu[1,2], Guanru Wu[1,2], Yanjing Zhang[1,2], Jinhui Shi[3], Wenjun Qu[1,2], Lifang Sheng[1,2], Wencai Wang[1,2], Daizhou Zhang[4], Yang Zhou[1,2]

[1]Frontier Science Center for Deep Ocean Multispheres and Earth System (FDOMES) and Physical Oceanography Laboratory, Ocean University of China, Qingdao 266100, China.

[2]College of Oceanic and Atmospheric Sciences, Ocean University of China, Qingdao 266100, China.

[3]College of Environmental Science and Engineering, Ocean University of China, Qingdao 266100, China.

[4]Faculty of Environmental and Symbiotic Sciences, Prefectural University of Kumamoto, Kumamoto 862-8502, Japan.

Correspondence to: Daizhou Zhang (dzzhang@pu-kumamoto.ac.jp) and Yang Zhou (yangzhou@ouc.edu.cn)

Abstract. Photocatalytic reactions during the daytime, alongside aqueous-phase reactions occurring during both daytime and nighttime, are identified as the two primary processes facilitating the conversion of aerosol iron (Fe) from the insoluble state to the soluble state within the atmospheric environment. This study investigated the levels of total Fe (Fe_T) and soluble Fe (Fe_S) in $PM_{2.5}$ samples collected during daytime and nighttime in Qingdao, a coastal city in eastern China, evaluating the distinctive roles of these two pathways in enhancing aerosol Fe solubility (%Fe_S, defined as the ratio of Fe_S to Fe_T). Under clean and humid conditions, characterized by prevailing sea breezes and a relative humidity (RH) typically above 80%, an average daytime %Fe_S of 8.7% was observed, which systematically exceeded the nighttime %Fe_S (6.3%). Photochemical conversions involving oxalate contributed to the higher %Fe_S observed during daytime. Conversely, in scenarios where air masses originated from inland areas and exhibited slightly polluted, daytime %Fe_S (3.7%) was noted to be lower than the nighttime %Fe_S (5.8%). This discrepancy was attributable to the variations in RH, with nighttime RH averaging around 77%, conducive to the more efficient generation of acidic compounds, thereby accelerating Fe_S production compared to the daytime, when RH was only about 62%. Furthermore, the oxidation rates of sulfur (SOR) displayed a strong correlation with RH, particularly when RH fell below 75%. A 10% increase in RH corresponded to a 7.6% rise in SOR, which served as the primary driver of the higher aerosol acidity and %Fe_S at night. These findings highlight the RH-dependent activation of aqueous-phase reactions and the augmentation of daytime photocatalysis in the formation of Fe_S in the coastal moisture atmosphere.

1 Introduction

Iron (Fe) plays a pivotal role as a micronutrient in marine ecosystems, being a critical component of atmospheric aerosol particles (Martin et al., 1994). Its deposition in high-nitrate, low-chlorophyll (HNLC) regions can trigger phytoplankton bloom, thus enhancing atmospheric carbon absorption and fixation in seawater (Watson et al., 1994; Watson and Lefévre, 1999; Toner, 2023). Notably, only the soluble fraction of Fe (Fe_S) in aerosols, referred to as bioavailable Fe, is accessible to phytoplankton (Zhuang et al., 1992; Sugie et al., 2013; Li et al., 2017). The proportion of Fe_S to the total aerosol Fe (Fe_T), i.e., the aerosol Fe solubility (%Fe_S), is influenced by the aerosols' sources and the chemical conversion of Fe from insoluble forms to soluble forms in the atmosphere. %Fe_S in fresh dust particles is typically below 1%, yet can exceed 10% in aerosols derived from combustion processes, such as fly ash from coal and oil combustion (Oakes et al., 2012; Shi et al., 2012; Wang et al., 2015; Li et al., 2022). The %Fe_S in primary particles can significantly increase due to atmospheric processes, primarily through aerosol acidification via aqueous-phase reactions or photochemical conversions of precursors of acidic species (Solmon et al., 2009; Shi et al., 2015; Li et al., 2017; Hettiarachchi et al., 2019), affecting the deposition flux of aerosol Fe_S over the open ocean (Chen and Siefert, 2004; Shi et al., 2013; Yang et al., 2020).

Solar radiation and ambient humidity are two key meteorological factors that greatly influence the processes of aerosol acidification. Solar irradiation induces photochemical reactions during daytime, leading to the formation of free radicals and accelerating the production of acidic species within aerosols, thereby facilitating Fe dissolution (Chen and Grassian, 2013; Liu et al., 2021b). Studies such as Fu et al. (2010) have demonstrated increased Fe_S in dust samples exposed to light in the HCl solution. Furthermore, daytime photolysis of Fe-organic complexes is another pathway for Fe_S formation, contributing to increased %Fe_S (Weller et al., 2014; Zhang et al., 2019; Zhou et al., 2020). For example, Zhou et al. (2020) and Zhang et al. (2019) reported that photolysis of oxalate-Fe(III) complex can result in the degradation of oxalate, enhancing Fe dissolution in aerosol particles during daytime. These mechanisms have been supported by laboratory experiments and model simulations (Zhu et al., 1993; Chen and Grassian, 2013; Sorooshian et al., 2013; Pang et al., 2019; Li et al., 2021). In contrast, high ambient relative humidity (RH) can facilitate the heterogeneous/liquid phase formation of sulfate and nitrate during nighttime, increasing aerosol acidity and promoting acids-associated Fe dissolution (Liu et al., 2020; Pye et al., 2020; Wong et al., 2020). Studies like Zhang et al. (2022) observed enhanced %Fe_S (>1%) at high RH levels (>60%) in winter, while Zhu et al. (2020) highlighted the greater impact of SO_4^{2-} and NO_3^- on %Fe_S at RH above 50%. Shi et al.

58 (2020) noted efficient Fe_S formation under foggy conditions, where SO_4^{2-} and NO_3^- concentrations were high due

59 to the absorption of precursor gases on wet particle surfaces, facilitating further water vapor absorption, and Fe_S

60 increase.

61 Aqueous-phase processes can occur during both daytime and nighttime, given adequate moisture. The formation

62 of Fe_S results from the interplay between photochemistry and aqueous chemistry during daytime, whereas it relies

63 solely on aqueous chemistry at night. The synergistic mechanisms and their individual contributions to Fe_S

64 formation remain partially understood.

65 To elucidate the roles of aqueous-phase and photochemical reactions on Fe_S formation, we collected $PM_{2.5}$ samples

66 during daytime and nighttime, separately, in a Chinese coastal city (Qingdao). Positioned under the westerlies of

67 the Northern Hemisphere, Qingdao acts as a primary conduit for East Asian terrestrial aerosols to the Northwestern

68 Pacific. Our research focuses on ascertaining the $\%Fe_S$ enhancement under clean and slightly-polluted air

69 conditions, reflecting typical coastal air quality. The primary goal is to delineate the contributions of aqueous-

70 phase reactions and photochemical processes to $\%Fe_S$ enhancement, thereby elucidating the dynamics of Fe

71 dissolution within the atmospheric chemistry of coastal areas.

72 **2 Methodology and materials**

73 **2.1 Sample collection and classification**

74 The observation was carried out on the following dates: April 24th to May 27th, 2017; March 28th to April 30th,

75 2018; and May 22nd to 28th, 2018. Two high-volume $PM_{2.5}$ samplers (TISCH, TE-6070BLX-2.5, USA) were

76 applied to collect $PM_{2.5}$ onto quartz microfiber filters (QM-A, PALL) and Whatman® 41 filters, respectively, on

77 the roof of Baguanshan Atmospheric Research Observatory (BARO, 36°03' N, 120°20' E, 76 m asl.). BARO is

78 located on the top of a small hill in the urban area of Qingdao, and around 0.7 km away from the coastline of the

79 Yellow Sea (Figure S1). $PM_{2.5}$ samples were collected separately during daytime and nighttime. Field blank

80 samples were also collected during the campaign by placing filters in the samplers with the samplers switched off.

81 After the sampling process, $PM_{2.5}$ samples were sealed and stored at $-20°C$ before analysis.

82 For the measurement of water-soluble ions (WSIs) and carbonaceous matters, aerosol samples collected on QM-

83 A filters were utilized. The samples collected on Whatman® 41 filters were used for the detection of elements.

84 Firstly, samples were cut into pieces and immersed in Milli-Q pure water. Then, water-soluble matters were

85 extracted by ultrasonic vibration at approximately 0°C for 40 min. The water extracts were then filtered through

86 syringes with 0.45 μm strainer heads (PALL). The filtered extracts were analyzed for WSIs, including Na^+, NH_4^+,

87 K^+, Mg^{2+}, Ca^{2+}, F^-, Cl^-, SO_4^{2-}, NO_3^-, $C_2O_4^{2-}$, using ion chromatography (IC, Dionex ICS-3000, Dionex Corp.,

88 Sunnyvale, CA, USA). Similar sample pretreatment procedures were used to determine soluble elements. While,

89 10 ml of filtrate was taken and 0.187 ml HNO_3 (mass fraction: 69%) was added to water extracts before measuring

90 soluble elements, in case soluble Fe(II) was oxidized into an insoluble state. To determine total elements, sample

91 pieces were placed into inner-tanks and subjected to digestion with a mixture of HNO_3 + HF (at a volume ratio of

92 4:1) at 180°C for 48 h. The element concentrations were measured using inductively coupled plasma mass

93 spectrometry (ICP-MS, Model: iCAP Qc, Thermo Fisher Scientific Inc., Germany). Carbonaceous materials,

94 specifically organic carbon (OC) and elemental carbon (EC), were analyzed using a sunset OC/EC analyzer from

95 Sunset Laboratory Inc. The detection limits of the analysis instruments used can be found in Table S1. The organic

96 matter (OM) content was estimated with 1.6 times OC, as proposed by Turpin and Lim (2001). Further details

97 about sample collection, pretreatment procedures, and chemical species detection can be found in our previous

98 work (Li et al., 2023a; Li et al., 2023b).

99 Various weather conditions and air pollution characteristics were encountered during the observation period,

100 including clean, slightly-polluted (SP), heavily-polluted, foggy, and dusty conditions. Due to the large deviations

101 and uncertainties in the statistical results of dust-related samples, data from these samples were not considered.

102 Additionally, samples from heavily-polluted periods (N = 6, defined by $PM_{2.5} > 50$ μg m^{-3} and $PM_{2.5}/PM_{10} > 0.4$)

103 and fog-influenced samples (N = 12) were also not included because of the limited sample number and the

104 significant difference in fog durations between samples. In this paper, we focus on the results of the clean period

105 samples (N = 19) and the SP period samples (N = 32). Clean periods samples were collected when $PM_{2.5} < 30$ μg

106 m^{-3} and $PM_{10} < 50$ μg m^{-3}. The SP periods samples were those collected when 30 μg $m^{-3} < PM_{2.5} < 50$ μg m^{-3} and

107 those collected when $PM_{2.5} < 30$ μg m^{-3} while $PM_{10} > 50$ μg m^{-3}.

108 **2.2 Aerosol pH and liquid water content**

109 ISORROPIA thermodynamic equilibrium model (version II, https://www.epfl.ch/labs/lapi/models-and-

110 software/isorropia/iso-code-repository/) was employed to estimate gas concentrations and aerosol water pH (Song

111 et al., 2018). The forward mode, which uses both gas and aerosol data as model input, was utilized for pH

112 calculations. This approach was preferred to the reverse mode because the later, using only aerosol data, is very

113 sensitive to the uncertainties of the measured WSIs concentrations (Hennigan et al., 2015; Song et al., 2018).

114   "Metastable-mode" was employed in ISORROPIA, assuming that solid precipitates did not form except for $CaSO_4$.

115   The concentrations of gaseous species (i.e., $NH_3(g)$, $HNO_3(g)$, $HCl(g)$) were not measured at the site. In alignment

116   with the approach proposed by Sun et al. (2018), we devised a strategy to estimate the concentrations of these

117   gaseous species. Initially, the input of aerosol data was assumed as the sum of aerosol and gas data (specifically

118   for HNO_3, HCl and NH_3). This step provided us with the first set of gas and aerosol data outputs. For the second

119   run, the gas data output derived from the initial run was added to the original aerosol data, and it was considered

120   as the sum of gas data and aerosol data just like the first run to calculate $HNO_3(g)$, $HCl(g)$ and $NH_3(g)$. The same

121   method was employed for subsequent iterations until the variance in the NO_3^- output below the 1% threshold in

122   mass. The calculation processes can be described by the following equations:

$$\text{Input}[C_{Aerosol}+C_{Gas}]_{N+1}=C_{Aerosol}+[C_{Gas}]_N \tag{1}$$

$$L = \left| \frac{[C_{NO_3^-}]_{N+1} - [C_{NO_3^-}]_N}{[C_{NO_3^-}]_N} \right| \times 100\% \tag{2}$$

125   where $C_{Aerosol}$ is the observed concentration of NO_3^- (or NH_4^+, Cl^-), C_{Gas} is the concentration of gaseous species

126   of $HNO_3(g)$ (or $NH_3(g)$, $HCl(g)$), and $[C_{Gas}]_N$ is the concentration of gaseous species of $HNO_3(g)$ (or $NH_3(g)$,

127      $HCl(g)$) output by ISORROPIA in the Nth run ($N \geq 1$). The iteration was stopped until $L < 1\%$.

128   Finally, three times of iterations ($N_{max} = 3$) were determined when $L = 0.1\%$. The aerosol pH was calculated by

129   using aqueous H^+ concentration and aerosol liquid water content (ALWC) outputted by ISORROPIA, as described

130   by equation (3).

$$pH = -\log_{10} \frac{1000 \times H^+(aq)}{ALWC} \tag{3}$$

132   Significant correlations between the results of the first run and the fourth run were observed for pH ($r^2 = 0.95$) and

133   ALWC ($r^2 = 0.99$), indicating the stability and reliability in estimating the pH and ALWC by ISORROPIA II

134   (Figure S2). Moreover, the correlations of NO_3^- ($r^2 = 0.71$), NH_4^+ ($r^2 = 0.98$) and Cl^- ($r^2 = 0.51$) between the

135   simulated results and measured concentrations are significant, demonstrating the robust confidence level of the

136   simulated results (Figure S3).

137   In addition, the impact of organic matter (OM) on aerosol pH was determined to be minimal. This can be attributed

138   to the limited sensitivity of the predicted pH to the water uptake by organic species ($ALWC_{org}$) when the OM

139   fraction in $PM_{2.5}$ is low (Guo et al., 2015; Liu et al., 2017). Following the methods of Guo et al. (2015), we

140 estimated ALWC$_{org}$ and its influence on aerosol pH. Our analysis determined the ALWC$_{org}$ to range between 0.83

141 and 3.31 μg m^{-3}, constituting merely 2.6−9.8% of the total ALWC. Aerosol pH was about 0.03−0.08 higher when

142 considering OM, affirming the negligible effect of OM on aerosol pH (see Text S1 in the supporting information

143 for more details).

2.3 Weather conditions and air quality data

145 The publicly released temperature, RH, surface pressure, wind speed, and wind direction recorded every 10

146 minutes were obtained from a meteorological observatory of the Qingdao Meteorological Bureau (Figure S1).

147 Hourly mass concentrations of PM$_{2.5}$, PM$_{10}$, SO$_2$, NO$_2$, O$_3$ and CO were obtained from an adjacent air quality

148 monitoring station in the Shinan District of Qingdao City (Figure S1), which is managed by Ministry of Ecology

149 and Environment of the People's Republic of China (http://www.mee.gov.cn/).

150 To examine the relative abundance of chemical species in aerosols, we reconstructed the mass concentrations of

151 PM$_{2.5}$ by equation (4) using the obtained concentrations of WSIs, OM, EC and elements.

$$PM_{2.5R} = WSIs + OM + EC + Elements + Si + Ca \tag{4}$$

153 where PM$_{2.5R}$ is the reconstructed PM$_{2.5}$, and WSIs consists of Na$^+$, NH$_4^+$, K$^+$, F$^-$, Cl$^-$, SO$_4^{2-}$, NO$_3^-$ and C$_2$O$_4^{2-}$. As

154 for elements, Mg, Al, V, Cr, Mn, Fe, Ni, Co, Cu, Zn, Ga, As, Se, Rb, Sr, Cd, Ba, Tl and Pb were considered. Si

155 and Ca concentrations were estimated based on the mass ratio of Si/Al (3.43) following the methodology described

156 by Huang et al. (2010) and the mass ratio of Ca/Al (0.80) suggested by Arimoto et al. (2004) and Wang et al.

157 (2011). Because the nearby monitoring station is closer to the sea and less affected by human activities (yellow

158 dot in Figure S1), the level of PM$_{2.5R}$ is higher than the observations from the monitoring station. But the trends of

159 variations of these two datasets were consistent, indicating the high confidence of the PM$_{2.5R}$ dataset. In addition,

160 any mention of ionic ratios or normalized parameters in the results and discussions of this paper indicates the data

161 was divided by PM$_{2.5R}$.

2.4 Provenances of air masses

163 The HYbrid Single-particle Lagrangian Integrated Trajectory (HYSPLIT) Model

164 (https://www.ready.noaa.gov/HYSPLIT.php), developed by NOAA, was applied to calculate the origins of air

165 masses from which PM$_{2.5}$ samples were collected. Gridded GDAS data with a horizontal resolution of 1.0° × 1.0°

166 were used as the input. Backward trajectories were computed for a period of 48 h, with starting points located at

167 300 m above ground level.

3 Results

3.1 Meteorological features of clean and SP periods

During clean periods, the backward trajectories reveal that the air masses mainly originated from sea areas (Figure 1). The prevailing sea breeze resulted in high RH levels of $81.5 \pm 4.9\%$ during daytime and $86.6 \pm 8.8\%$ during nighttime (Table 1). The minimal temperature variance of about 2℃ between daytime and nighttime further reflects the characteristics of marine atmosphere. In contrast, air masses during SP periods originated from various directions, with a significant number traversing terrestrial regions prior to arriving at the collection site. Temperature and RH exhibited noticeable diurnal variations. The daytime temperature was 17.2 ± 3.0℃ and decreased to 13.2 ± 3.7℃ during nighttime. The RH levels were $62.1 \pm 9.4\%$ and $76.8 \pm 9.4\%$ during daytime and nighttime, respectively.
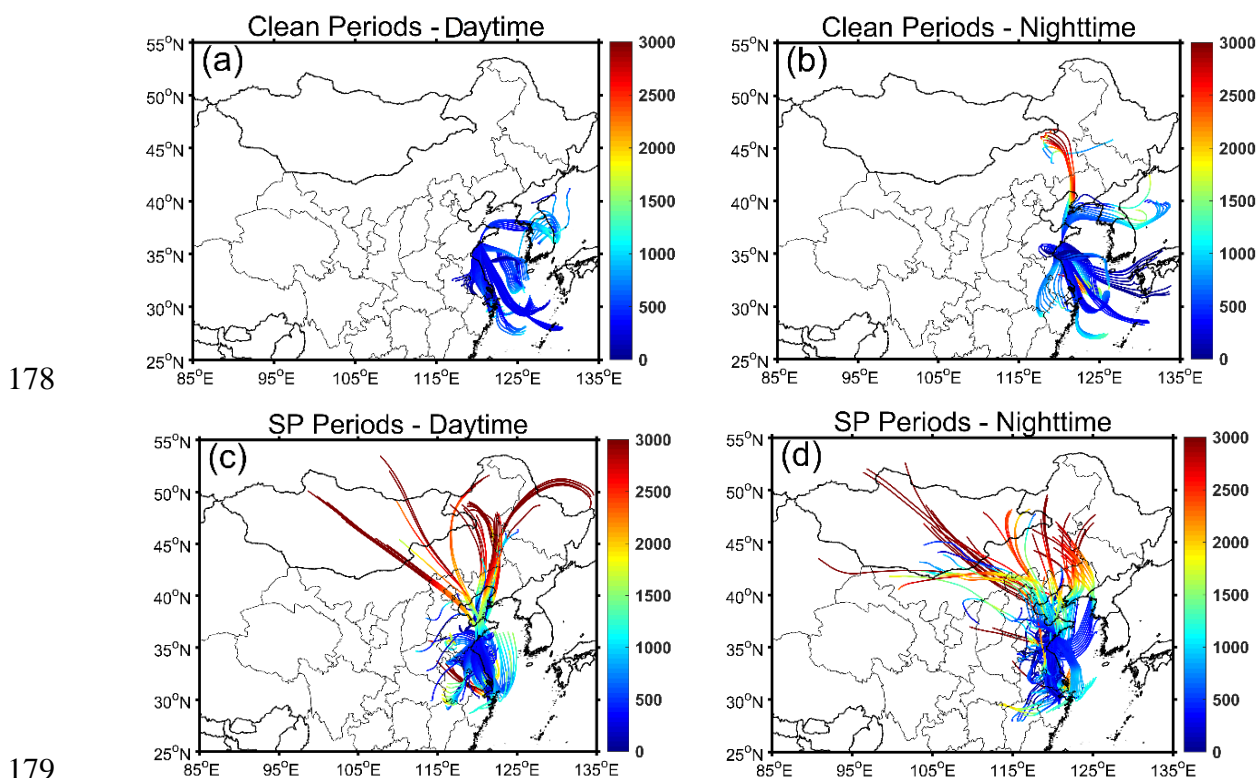
Figure 1: 48-h backward trajectories during daytime and nighttime during clean and slightly-polluted (SP) periods. Trajectories are color-coded based on the altitude (unit: m) above the ground.

3.2 Concentrations of PM$_{2.5}$ and Fe, and %Fe$_S$

Table 1 presents the PM$_{2.5}$ levels and aerosol Fe concentrations during both clean and SP periods. Under clean conditions, PM$_{2.5}$ concentrations were similar during daytime and nighttime, with average values of 16.9 μg m^{-3} and 16.4 μg m^{-3}, respectively. Compared to the nighttime, Fe$_T$ and Fe$_S$ concentrations were higher during the

daytime, which were 289.2 ± 223.4 ng m^{-3} and 20.0 ± 10.5 ng m^{-3}, respectively. Daytime levels of Fe$_T$ and Fe$_S$ were 1.5 times and 1.6 times as high as those observed at night, respectively. The increase in Fe$_T$ and Fe$_S$ during daytime may be linked to heightened human activities. Furthermore, the elevated Fe$_S$ during daytime could be attributed to photochemical processes, which promoted the dissolution of aerosol Fe, a topic to be discussed further in Section 4.2. %Fe$_S$ values ranged from 2.3% to 14.1% with an average of 8.7% during daytime, approximately 1.4 times the nighttime average of 6.3% (after removing an extreme point of 37.2%).

Table 1. Meteorological parameters, %Fe$_S$, aerosol pH, the concentrations (average ± standard deviation) of PM$_{2.5}$ and chemical species during clean and slightly-polluted periods.

	Clean Periods		Slightly-polluted Periods	
	Daytime	Nighttime	Daytime	Nighttime
PM$_{2.5}$ (μg m^{-3})	16.9 ± 3.1	16.4 ± 5.6	30.3 ± 7.0	28.3 ± 7.7
Temperature (°C)	16.6 ± 2.8	14.3 ± 2.3	17.2 ± 3.0	13.2 ± 3.7
RH (%)	81.5 ± 4.9	86.6 ± 8.8	62.1 ± 9.4	76.8 ± 9.4
ALWC (μg m^{-3})	30.0 ± 13.5	55.0 ± 53.7	22.5 ± 13.2	44.1 ± 33.8
Fe$_T$ (ng m^{-3})	289.2 ± 223.4	186.7 ± 122.2	938.3 ± 850.5	520.3 ± 496.1
Fe$_S$ (ng m^{-3})	20.0 ± 10.5	12.5 ± 7.4	25.7 ± 10.5	21.6 ± 8.1
%Fe$_S$ (%)	8.7 ± 3.8	6.3 ± 4.1	3.7 ± 2.0	5.8 ± 3.0
pH	0.46 ± 0.83	1.06 ± 0.96	1.16 ± 0.88	0.98 ± 0.75
SO$_4^{2-}$ (μg m^{-3})	13.97 ± 5.19	10.97 ± 8.06	14.94 ± 5.81	13.78 ± 5.43
F(SO$_4^{2-}$)[a]	42.9% ± 14.0%	36.8% ± 14.0%	20.9% ± 3.6%	23.0% ± 5.3%
NO$_3^-$ (μg m^{-3})	5.82 ± 3.49	5.63 ± 4.87	26.71 ± 13.15	22.80 ± 10.81
F(NO$_3^-$)[b]	15.7% ± 6.0%	17.7% ± 11.3%	35.4% ± 9.0%	35.6% ± 9.0%
(2[SO$_4^{2-}$]+[NO$_3^-$])/PM$_{2.5R}$ (μmol μg^{-1})	0.0115 ± 0.0026	0.0105 ± 0.0023	0.0101 ± 0.0017	0.0106 ± 0.0016

[a] F(SO$_4^{2-}$) is the fraction of SO$_4^{2-}$ in PM$_{2.5}$ mass, which was calculated by using SO$_4^{2-}$ concentrations divided by PM$_{2.5R}$ concentrations. [b] F(NO$_3^-$) is the fraction of NO$_3^-$ in PM$_{2.5}$ mass. The calculation method is the same as F(SO$_4^{2-}$).

Under SP conditions, PM$_{2.5}$ was at similar levels during daytime and nighttime with the average values of 30.3 μg m^{-3} and 28.3 μg m^{-3}, respectively. However, the daytime Fe$_T$ (938.3 ± 850.5 ng m^{-3}) was much higher than the nighttime Fe$_T$ (520.3 ± 496.1 ng m^{-3}), which was approximately threefold higher than during clean periods. Similarly, the daytime Fe$_S$ concentration of 25.7 ± 10.5 ng m^{-3} was also slightly higher than the nighttime concentrations of 21.6 ± 8.1 ng m^{-3}, which was 1–2 times higher than that during the clean period. Different from

the clean period, %Fe$_S$ was markedly higher at night (5.8% $\pm$ 3.0%) compared to the daytime %Fe$_S$ (3.7% $\pm$ 2.0%)

during the SP period, ranging from 1.0% to 12.3%.

3.3 Chemical characteristics of PM$_{2.5}$

Figure 2 illustrates the mass fractions of various chemical species present in the reconstructed PM$_{2.5}$ (PM$_{2.5R}$). During the clean period, WSIs were the dominant components, constituting about 75.0% and 74.1% of PM$_{2.5}$ mass during daytime and nighttime, respectively. SO$_4^{2-}$, NO$_3^-$, and NH$_4^+$ were the main contributors to WSIs. During daytime, SO$_4^{2-}$ and NO$_3^-$ were 13.97 $\pm$ 5.19 μg m^{-3} and 5.82 $\pm$ 3.49 μg m^{-3}, respectively, serving as the major acidic species and accounting for 42.9% and 15.7% of the PM$_{2.5}$ mass (Table 1 and Figure 2). At night, SO$_4^{2-}$ and NO$_3^-$ concentrations decreased slightly, which were 10.97 $\pm$ 8.06 μg m^{-3} and 5.63 $\pm$ 4.87 μg m^{-3}, respectively, representing 36.8% and 17.7% of the PM$_{2.5}$ mass (Table 1 and Figure 2). In other words, the two main acid species, SO$_4^{2-}$ and NO$_3^-$, occupied slightly larger fractions of the PM$_{2.5}$ mass during the daytime (58.7%) compared to the nighttime (54.6%), along with the lower ALWC, resulting in the lower aerosol pH of 0.46 $\pm$ 0.83 during daytime (Table 1). At night, aerosol pH (1.06 $\pm$ 0.96) increased by a factor of 2.3 compared to daytime.

The aerosol pH calculated in this work was evidently lower than many other areas of China (Liu et al., 2017; Wang et al., 2019; Xu et al., 2020). During the clean period, air masses mainly originated from the seas. Therefore, the aerosol pH can be very acidic because of the lack of sources of alkaline substances over the ocean, such as NH$_3$, Ca^{2+}, et al. (Zhou et al., 2018). Compared to the inland areas, much lower aerosol pH in coastal areas is reasonable (Wang et al., 2022). For instance, Zhou et al. (2018) reported that the pH of aerosols near the Bohai Sea can be as low as around 1.0. Moreover, they also found that the daytime aerosol acidity was significantly stronger than that during the nighttime in coastal areas. This observation aligns with the findings during clean periods in our study, which were characterized by the predominance of sea breezes. In this study, we employed the ratio of acidic substances to PM, namely, (2[SO$_4^{2-}$] + [NO$_3^-$])/PM$_{2.5R}$, to characterize the level of acidic substances in a unit of PM$_{2.5}$, because SO$_4^{2-}$ and NO$_3^-$ were predominant acidic species within WSIs (>75% in mass). It was 0.0115 $\pm$ 0.0026 μmol μg^{-1} and 0.0105 $\pm$ 0.0023 μmol μg^{-1} in PM$_{2.5}$ mass during daytime and nighttime, respectively (Table 1).
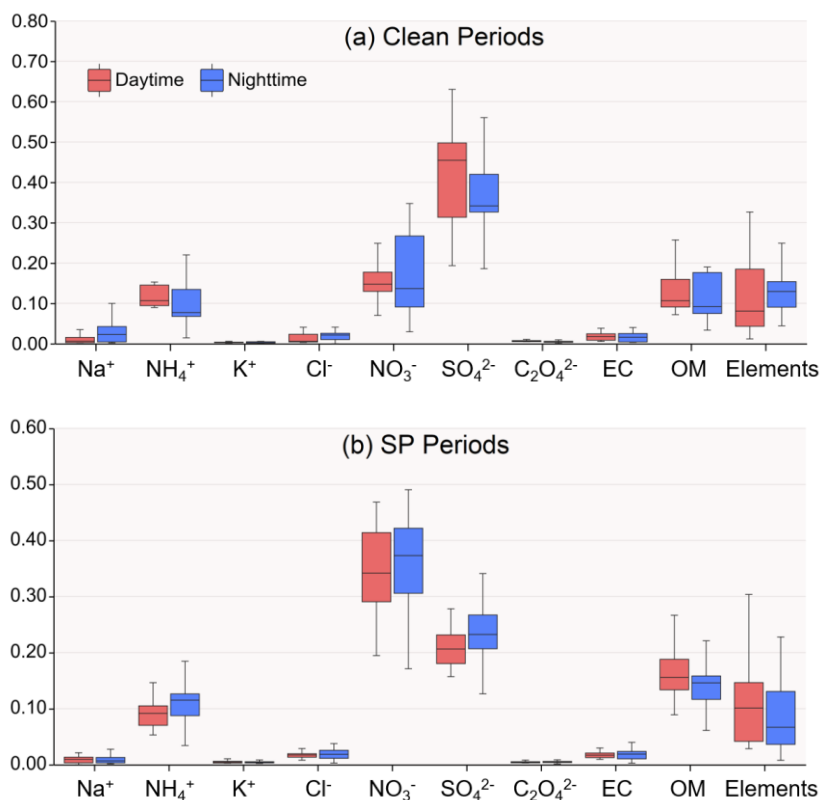
228

229

230 **Figure 2: Mass fractions of chemical species in reconstructed PM₂.₅ mass during daytime and nighttime in clean and SP**

231 **conditions. Mg²⁺ and Ca²⁺ are not shown in the above pictures, because total Mg is included in elements data and total**

232 **Ca is assessed by 0.8 times Al.**

233

234 During the SP period, WSIs retained similar proportions in $PM_{2.5}$ as during the clean period, accounting for 70.5%

235 and 74.3% during daytime and nighttime, respectively. SO_4^{2-}, NO_3^-, and NH_4^+ were also the main contributors to

236 WSIs. In the daytime, the concentrations of SO_4^{2-} and NO_3^- were 14.94 ± 5.81 µg m⁻³ and 26.71 ± 13.15 µg m⁻³,

237 respectively, showing a marginal elevation over nighttime levels (Table 1). However, SO_4^{2-} had evidently lower

238 contributions to $PM_{2.5}$ compared to the clean period, which were only 20.9% and 23.0% during daytime and

239 nighttime, respectively (Table 1 and Figure 2). In contrast, NO_3^- had a noticeably higher contribution to $PM_{2.5}$

240 compared to the clean period, exhibiting little diurnal variation, with percentages of 35.4% and 35.6% during

241 daytime and nighttime, respectively (Table 1 and Figure 2). In total, the ratio of acids to PM (i.e.,

242 $(2[SO_4^{2-}]+[NO_3^-])/PM_{2.5R})$ was 0.0101 ± 0.0017 µmol µg⁻¹ during daytime and 0.0106 ± 0.0016 µmol µg⁻¹ during

243 nighttime (Table 1). Even though the ALWC (44.1 ± 33.8 µg m⁻³) was significantly more abundant at night

244 compared to the daytime (22.5 ± 13.2 µg m⁻³), the aerosol pH was lower at night. Specifically, the nighttime

245 aerosol pH was 0.98 ± 0.75, while the daytime aerosol pH was slightly higher at 1.16 ± 0.88, indicating weaker

246 aerosol acidity during daytime with a 18.4% increase in pH compared to nighttime aerosols.

4 Discussion

We found that daytime %Fe$_S$ was much higher than nighttime %Fe$_S$ during the clean period, while the opposite pattern emerged during the SP period. This section delves into the primary factors driving the distinct diurnal shifts in aerosol %Fe$_S$ during clean and SP periods, based on the aspects of aqueous-phase conversions and photocatalysis reactions.

4.1 Aqueous-phase conversions promoted by acid processes

The %Fe$_S$ was dependent on the acidification of the aerosol particles, and high %Fe$_S$ was associated with low aerosol pH (Table 1). The pH of aerosols is controlled by ALWC and H$^+$ contents. The predominant acidic species, i.e., SO$_4^{2-}$ and NO$_3^-$, play crucial roles in promoting the dissolution of insoluble Fe through proton-promoted reactions. As shown in Figure 3a, there was a significant negative correlation between the aerosol pH and the relative content of these two acidic species when the pH was below 4. Especially during clean and SP periods (r = 0.62, Figure 3a), the slope of the regression line was approximately –602.99, indicating that a variation of 1.0 nmol μg^{-1} of the acidic species content in PM$_{2.5}$ can lead to a noticeable fluctuation of aerosol pH (about 0.60). For instance, the daytime aerosol pH was 0.60 lower than that of the nighttime during the clean period, even though the difference of the two acidic species content was only about 1.0 nmol μg^{-1}.
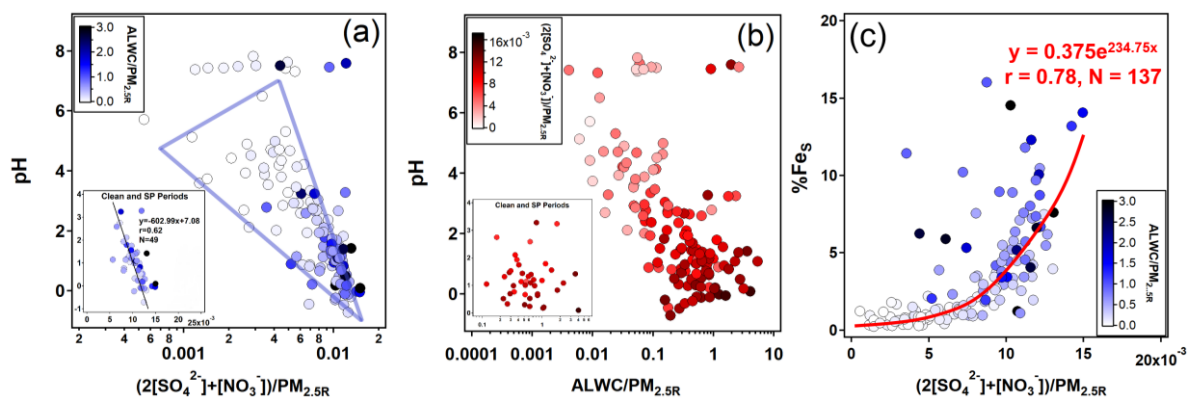
Figure 3: Relationships among pH, the normalized relative abundance of ALWC (unit: μg m^{-3}) and main acidic species (= 2[SO$_4^{2-}$] + [NO$_3^-$], unit: μmol m^{-3}) with respect to the reconstructed PM$_{2.5}$ (i.e., PM$_{2.5R}$, unit: μg m^{-3}), and %Fe$_S$. The subgraph at the bottom-left of figures (a) and (b) show scatter plots during clean and SP periods with the linear regression line obtained by using the Igor Pro-based program developed by Wu and Yu (2018).

There was no prominent correlation between pH and ALWC when the pH exceeded 6 (Figure 3b). When the pH was smaller than 6, the increasing ALWC facilitated the heterogeneous reactions of SO$_2$ and NO$_2$ to generate more

270   SO_4^{2-} and NO_3^-, lowering the aerosol pH and enhancing the %Fe$_S$. The formation of SO_4^{2-} and NO_3^- will further

271   facilitate the growth of ALWC due to their remarkable hygroscopicity, establishing a positive feedback (Path A in

272   Figure 4), referred to as the "ALWC-acid" feedback (Wang et al., 2016; Wu et al., 2018b). On the other hand,

273   ALWC dilutes H^+ in aerosol water. This process weakens the aerosol acidity and inhibits the particles from %Fe$_S$

274   elevation (Path B in Figure 4). In addition, the increasing ALWC served as a medium for loading water-soluble

275   components may promote the formation of Fe$_S$ (Path C in Figure 4). The profound influence of acidic species on

276   the aerosol pH indicates the predominance of the "ALWC-acid" feedback in modulating the aerosol pH and

277   augmenting %Fe$_S$ (Figures 3a, 3c and S4). The high %Fe$_S$ we observed during daytime and nighttime can be

278   attributed to the relatively higher content of acidic species in PM$_{2.5}$.
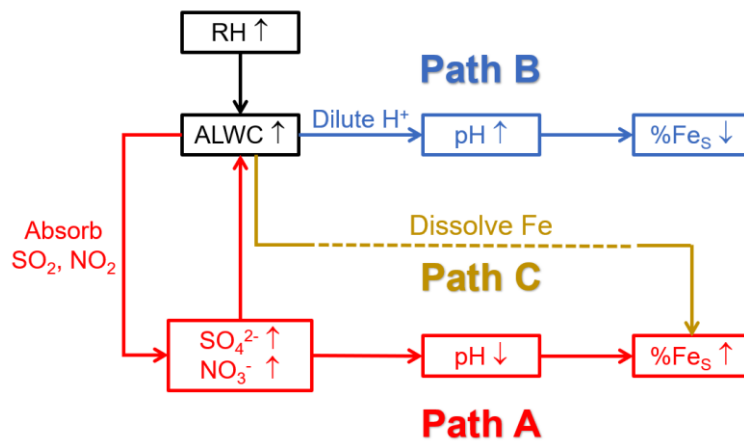
279

280   **Figure 4: Schematic diagram of ALWC affecting pH and %Fe$_S$. Path C is challenging to observe and quantify because**

281   **of the Fe$_S$ extraction using MilliQ water in the sample pretreatment.**

282

283   RH is a key factor in the formation of SO_4^{2-} and NO_3^- through heterogeneous/aqueous-phase reactions within

284   aerosols (Wang et al., 2016; Liu et al., 2020; Hou et al., 2022). As demonstrated in Figure 5, the strong dependency

285   of the oxidation rate of sulfur (SOR, defined as $[SO_4^{2-}]/([SO_4^{2-}] + [SO_2])$) on RH was observed under moderate

286   humid conditions (r = 0.64, p < 0.01). But the oxidation rate of nitrogen (NOR, defined as $[NO_3^-]/([NO_3^-] + [NO_2])$)

287   had a poor dependence on RH (r = 0.46, p > 0.05). A decrease of 10% in RH resulted in a notable reduction of

288   7.6% in SOR (Figure 5). Such a striking RH dependence was observed mainly during the SP period, indicating the

289   significant role of heterogeneous reactions in controlling the formation of SO_4^{2-}. Therefore, the facilitation of

290   aqueous-phase conversions leading to the formation of SO_4^{2-} was more pronounced at night during the SP period,

291   attributed to the high RH. This, in turn, resulted in a high proportion of SO_4^{2-} and acidic species, as well as the

elevated SOR (Table 1, Figures 2b and S5). The nighttime aerosol pH was approximately 0.18 units lower than that during daytime, but this slight variation did not hinder the efficient formation of Fe_S during nighttime in SP periods.

In contrast, RH was generally above 80% during daytime and nighttime in clean periods. The SOR was 0.49 on average and did not exhibit a clear correlation with RH beyond 78% (Figure 5a). Similar phenomena have been observed in previous studies, suggesting the existence of a saturation point in the promotion of RH on the aqueous-phase formation of SO_4^{2-} (Wang et al., 2019; Wang et al., 2021). High RH ($> 70\%$) can cause water-soluble species to deliquesce and form an aqueous layer on the particle surface. Once the aqueous layer forms, the influence of RH variations becomes minimal (Shi et al., 2022). Hence, the degree of aqueous-phase processes promoting SO_4^{2-} formation during clean periods was similar across both daytime and nighttime.
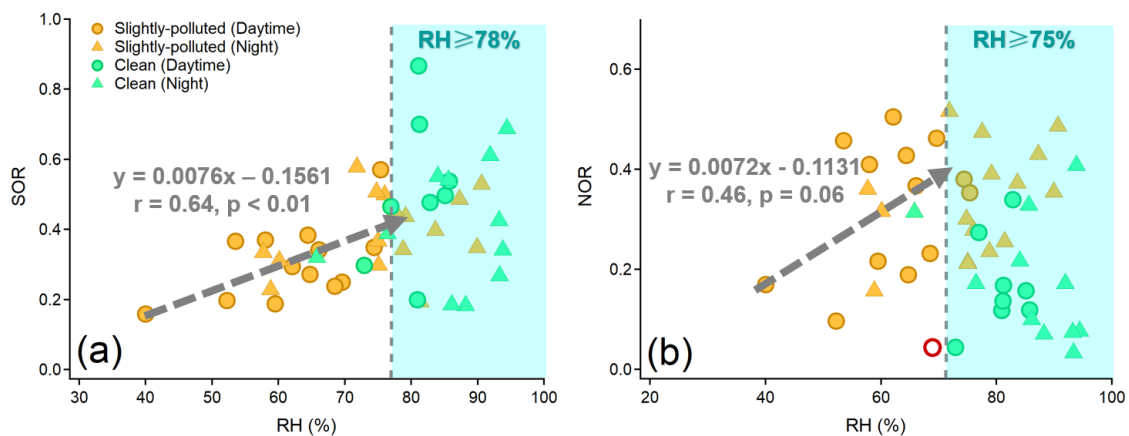
Figure 5: The dependence of SOR (a) and NOR (b) on RH during clean and slightly-polluted periods. The fitting of the regression line between SOR and RH was fitted when RH<78%. The fitting of the regression line between NOR and RH was fitted when RH<75% and one deviation point (the red circle in (b)) was removed.

4.2 Daytime enhancement by photocatalysis reactions

4.2.1 The influence of photochemical processes on sulfate formation

Photochemical reactions can enhance the formation of acidic species and increase the aerosol $\%Fe_S$ through aerosol acidification (Tao et al., 2020; Liu et al., 2021a). The large proportion of acidic species during the daytime of the clean period was attributable to SO_4^{2-}, which was 6.1% higher than the nighttime SO_4^{2-} (Table 1 and Figure 2a). Despite similar levels of SO_2 observed during daytime and nighttime, the daytime SOR reached as high as $0.50 \pm$

313   0.20 (Figure S5). The conversion rates in the aqueous phase were similar during daytime and nighttime in clean

314   periods. Therefore, the substantial fraction of SO_4^{2-} was most likely caused by photochemical reactions.

315   O_x (described by the sum of O_3 and NO_2) was investigated to quantify the potential of photochemical reactions,

316   following the method of Wu et al. (2018a). The daytime O_x concentration (56.1 ± 6.4 ppb) was about 5.1% higher

317   than that of nighttime O_x (53.4 ± 9.3 ppb) during the clean period. The substantial SOR occurred under the extreme

318   O_x conditions (Figure 6a), suggesting a significant contribution of the photochemical reactions during the clean

319   period. The enhancement of daytime photochemistry and aqueous chemistry on aerosol %Fe$_S$ was more

320   pronounced than that of the nighttime aqueous reactions solely during the clean period (Figure 7a and 7b).
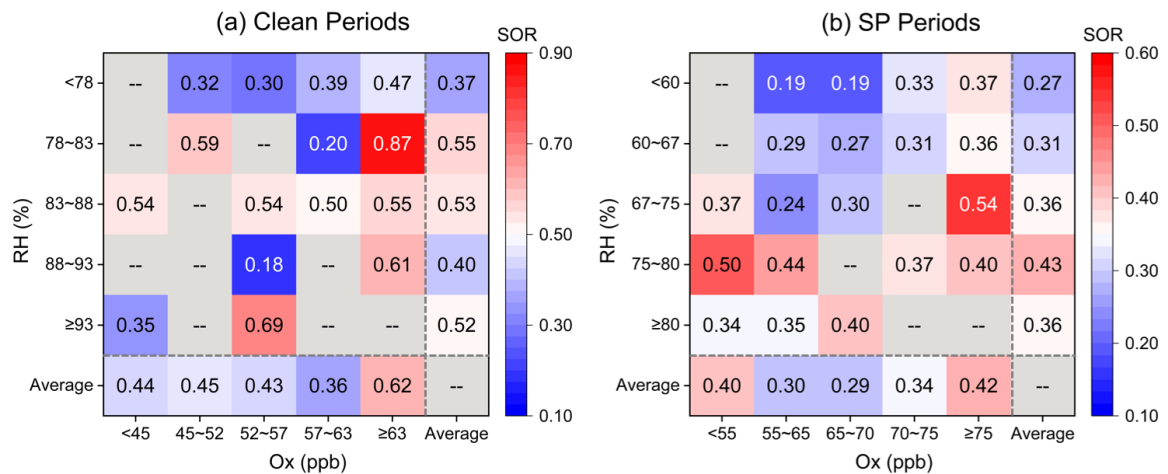
322 **Figure 6: RH-O$_X$ image plots colored by SOR during clean and SP periods. The last rows and columns of the matrices**

323 **represent the average value of SOR in the corresponding ranges of RH and O$_X$.**

325   During the SP period, the extent of SOR was more influenced by RH than by O_x, especially when RH was below

326   80% (Figure 6b). Nighttime SOR (0.37 ± 0.12) was approximately 1.2 times higher than the daytime SOR ($0.31 \pm$

327   0.11) even though the daytime O_x was higher than that during nighttime (Figure S5), indicating a greater

328   contribution of liquid/heterogeneous reactions to the SO_4^{2-} formation than photocatalytic reactions. Similar

329   findings were reported by Hou et al. (2022), who highlighted the dominant role of humidity rather than O_x in SO_4^{2-}

330   formation in haze intensification. The nighttime exhibited a more significant "ALWC-acid" feedback compared to

331   the daytime during the SP period. The influence of daytime photochemistry combined with aqueous-phase

332   reactions was comparatively weaker than nighttime aqueous chemistry, leading to the higher %Fe$_S$ at night (Figure

333   7c and 7d). Notably, O_x concentrations were significantly higher during the SP period in comparison to the clean

334   period (Figure S5), indicating more active daytime photocatalytic reactions. However, the impact of aqueous-

335   phase conversions during the SP nighttime period was relatively weak compared to the nighttime of the clean

336   period. These results suggest that the role of photocatalytic reactions in SO_4^{2-} formation, and subsequently in the

337   elevation of aerosol %Fe_S, was feeble compared to aqueous-phase conversions.
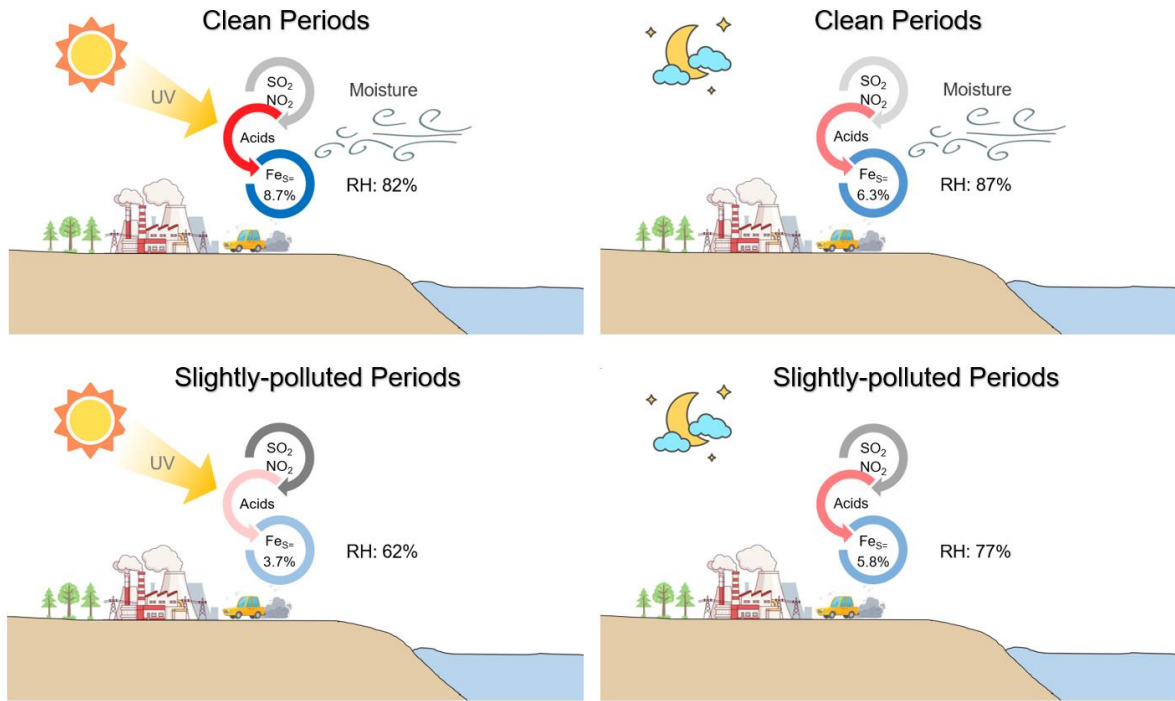
338

339   **Figure 7: Conceptual diagram showing the Fe dissolution influenced by acid processes at the coastal city during daytime**

340   **and nighttime in clean and SP periods.**

341

342   Enhancing aerosol %Fe_S through direct photocatalysis pathways is indeed possible. Iron oxides in minerals can

343   generate conduction band electrons upon irradiation, causing the reductive dissolution of Fe(III)-containing solid

344   phases to Fe(II) species (Zhang et al., 1993; Fu et al., 2010). However, structural Fe(III), which is the major iron-

345   related mineral in dust and coal fly ash, does not readily undergo direct reduction upon UV irradiation (Fu et al.,

346   2012; Fu et al., 2010; Xie et al., 2020). Another pathway for photolysis-conduced iron dissolution involves the

347   reduction by reactive oxygen species (ROS, e.g., $O_2^{\bullet-}$, $HO_2^{\bullet}$, and H_2O_2). These ROS can be generated from

348   dissolved oxygen accompanied by conduction band electrons, enhancing the Fe dissolution by reducing the solid-

349   phase Fe(III) into the more soluble Fe(II) form (Zhu et al., 1997; Hettiarachchi and Rubasinghege, 2020). Aerosol

350   water is necessary for the above reactions, and the proton-promoted dissolution by acid species is indispensable to

351   dissolve the solid-phase Fe(II) into aerosol solutions. We suppose that the observed weak influence of

photocatalysis on %Fe$_S$ was because of the extreme aerosol acidity. The acidity of aerosols, such as a pH as low as 2.0 during daytime of the present study, can suppress the contribution of photochemical catalysis in the formation of Fe$_S$ (Zhu et al., 1993; Fu et al., 2010; Fu et al., 2012). In addition, studies have suggested that Fe dissolution can be inhibited in H$_2$SO$_4$ systems under irradiation compared to dark conditions, which could be another reason for the low %Fe$_S$ during daytime although the exact mechanism remains unclear (Fu et al., 2010; Hettiarachchi et al., 2018).

4.2.2 The enhancement of %Fe$_S$ promoted by oxalate-related conversions

Oxalate can form complexes with Fe(III) and participate in photochemical reactions through photoinduced charge transfer. Oxalate transfers its charge to the Fe(III) surface via photolytic reactions during daytime, resulting in the reduction of Fe(III) to Fe(II), followed by the dissociation of the formed Fe(II) from the surface and hence the dissolution of aerosol Fe (Zuo and Hoigne, 1992; Zhang et al., 2019; Lueder et al., 2020). Shi et al. (2022) identified the oxalate/Fe$_T$ ratio as an excellent predictor for aerosol %Fe$_S$ through machine learning, underscoring its remarkable effectiveness. However, field observations rarely confirm its influence on Fe$_S$ from the perspective of oxalate-Fe photochemistry.
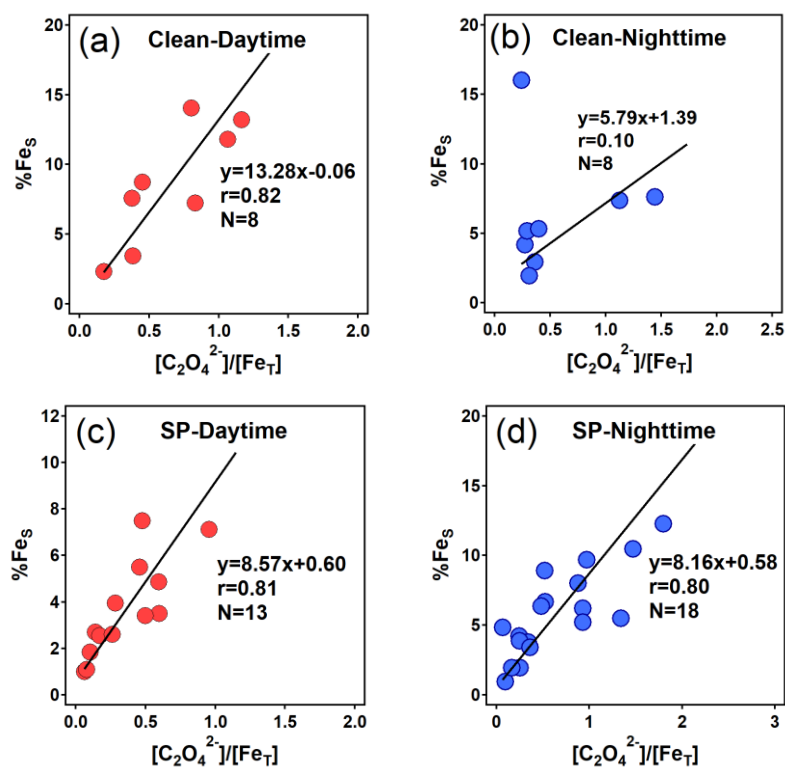
Figure 8: Relationships between %Fe$_S$ and the molar ratio (unit: μmol μmol^{-1}) of oxalate to Fe$_T$ during daytime and nighttime in clean and SP periods. An extreme point (%Fe$_S$ = 37.2%) in (b) was removed.

370

371 In this study, significant correlations were observed between %Fe$_S$ and the molar ratio of [oxalate]/[Fe$_T$] during

372 daytime in both clean periods (r = 0.82) and SP periods (r = 0.81) (Figure 8a and 8c). Similarly, a striking

373 correlation was also found in nighttime during the SP period (r = 0.80), although with a lower slope of 8.16 in the

374 regression line (Figure 8d). Noteworthy is the strong dependence of %Fe$_S$ (or Fe$_S$) on oxalate concentration at

375 night (Figures 8d, S6b and S6d). Field observations highlight the pivotal role of organic compound complexation

376 in stabilizing Fe (Sakata et al., 2022). Additionally, as illustrated by Figure 8a and 8c, the variation in %Fe$_S$ induced

377 by each unit variation in daytime [oxalate]/[Fe$_T$] was greater than its nighttime equivalent. The most notable

378 increase was observed during the clean period, with a daytime slope of 13.28, marking a 1.5-fold increase over the

379 SP period (daytime slope = 8.57). Similarly, the concentration of Fe$_S$ per unit of oxalate showed a parallel trend,

380 marking the highest daytime slope of the clean period during the campaign (Figure S6). Such patterns imply that

381 enhanced sunlight in clean days may have catalyzed photochemical processes involving daytime oxalate-Fe,

382 leading to elevated Fe$_S$ and %Fe$_S$. While these outcomes have only been discussed through laboratory simulations

383 (Chen and Grassian, 2013), or indirectly by examining oxalate degradation or sulfate formation (Zhou et al. 2020),

384 and they have been empirically discovered through field observations now in this study.

385 Simultaneously, Fe$_S$ species redox reactions can facilitate the formation of oxalate in return if the precursors are

386 abundant, particularly with aqueous-phase reactions playing a pivotal role when RH exceeds 60% (Zhang et al.,

387 2019). This may elucidate one of the main reasons behind the significant correlations observed between Fe$_S$ and

388 oxalate. Notably, oxalate concentration was higher during the daytime compared to the nighttime in this study

389 (Figure S5), concomitant with elevated Fe$_S$ concentrations. The photocatalytic degradation of oxalate-Fe,

390 promoting Fe dissolution during daytime, was unlikely to be the predominant pathway influencing the oxalate

391 concentration, otherwise a decrease in oxalate concentration would occur (Dou et al., 2021). Therefore, the oxalate

392 formation process catalyzed by Fe$_S$ could yield a higher production rate of oxalate during the daytime than at night.

393 Figure S7 portrays the conceptual diagram of these conversion processes. Similar scenarios might unfold for SO_4^{2-}

394 formation due to the heightened Fe redox reactions during daytime (Zhou et al., 2020). Owing to the extremely

395 low aerosol pH (< 2), transition-metal ions (TMIs, e.g., Fe$_S$)-catalyzed pathway could primarily influence the

396 secondary formation of SO_4^{2-}, leading to potent aerosol acidity (Liu et al., 2021b). The elevated aerosol acidity, in

397   turn, fostered the formation of Fe_S, thus furthering the generation of SO_4^{2-} and oxalate under high RH conditions.

398   The resulting oxalate could then be complexed with Fe_S, sustaining %Fe_S at a high level at night.

399   To summarise, the findings of this study suggest that daytime photochemical processes indeed facilitated the

400   dissolution of aerosol Fe, consequently elevating %Fe_S during the clean period. This mechanism, in turn, may

401   foster the secondary formation of oxalate and SO_4^{2-}. The complexation of organic compounds significantly

402   contributed to maintaining the high %Fe_S at night. While during SP periods, the diurnal variation in aerosol %Fe_S

403   mainly resulted from the differing levels of aerosol acidity between daytime and nighttime rather than oxalate-

404   related conversions, a conclusion strongly supported by the higher %Fe_S observed at night compared to daytime

405   (Figure 8c and 8d).

406   **4.3 Environmental implications**

407   Limited research has explored the diurnal variation of aerosol %Fe_S. Only an early case investigated the diel

408   variability of Fe species at an island located in the Caribbean Sea and highlighted the photochemical processing

409   of Fe (Zhu et al., 1997). This study found a pronounced correlation between Fe_S and acid species within an aerosol

410   pH range of 0 to 1, emphasizing the considerable influence of aerosol acidification on Fe dissolution. These

411   findings align with the results of our study. Our results suggest that acid-driven aqueous-phase transformations

412   could have a more crucial role in altering aerosol %Fe_S than photochemical reactions under certain conditions in

413   coastal urban areas.

414   Previous studies pinpointed robust %Fe_S of anthropogenic aerosols, especially for combustion-related fly ash

415   (Oakes et al., 2012; Wang et al., 2015; Baldo et al., 2022; Li et al., 2022). Unlike urban air, RH tends to be

416   considerably higher over open oceans, fostering an environment where heterogeneous reactions and the secondary

417   formation of SO_4^{2-} and NO_3^- are prevalent. In such cases, photochemical reactions and precursors' concentrations

418   will determine the formation of salts. Given that the air mass of the clean period comprised a mix of marine and

419   local urban air, it is expected that the Fe dissolution in aerosol particles is an effective way to produce Fe_S during

420   daylight hours. Air masses moving from densely populated land areas carry substantial amounts of SO_2, NO_2 and

421   NH_3 to offshore areas, aiding in the formation of SO_4^{2-} and NO_3^- and conducing to the acidic dissolution of Fe in

422   aerosol particles. Subsequently, the solubilized Fe, through proton-promoted dissolution, can be further stabilized

423   by the organic complexation of Fe in the marine atmosphere, as indicated by Sakata et al. (2022).

424 Additionally, the dearth of ammonia sources in the marine atmosphere may hinder the formation of SO_4^{2-} and

425 NO_3^- to some extent on the one hand (Wang et al., 2017; Guo et al., 2018). The limited availability of ammonia

426 may be also conducive to enhancing the aerosol acidity and elevating aerosol $\%Fe_S$ on the other hand. Considering

427 that concentrations of HCl in remote marine atmospheric boundary layer are typically higher than in the continent

428 of East Asia, the influence of chloride on aerosol pH may therefore play a conspicuous role in regulating $\%Fe_S$

429 (Tobo et al., 2010), on which knowledge is very limited.

430 **5 Summary**

431 This study investigated the daytime and nighttime $\%Fe_S$ in $PM_{2.5}$ in a coastal city of China under clean and SP

432 conditions. Under clean conditions, $\%Fe_S$ was higher during daytime (8.7%) compared to the nighttime (6.3%,

433 after removing an extreme point of 37.2%). On the contrary, under SP conditions, $\%Fe_S$ was higher at night (5.8%)

434 than during daytime (3.7%). Significant correlations were observed between the main acidic components (SO_4^{2-}

435 and NO_3^-), aerosol pH, and $\%Fe_S$, indicating that the acid process played a dominant role in influencing

436 aerosol $\%Fe_S$.

437 The RH consistently exceeded 80% during both daytime and nighttime in clean periods. Aqueous-phase reactions

438 were found to be most effective in promoting the secondary formation of acid species, with photochemical

439 processes further enhancing SO_4^{2-} formation during daytime. Together with the lower ALWC, the aerosol pH was

440 much lower during daytime (0.46 ± 0.83) compared to nighttime (1.06 ± 0.96) during the clean period, which

441 exerted a more significant influence on aerosol Fe dissolution. In contrast, RH was much higher at night (76.8%)

442 than that during daytime (62.1%) in the SP period. The dry conditions during daytime notably restricted the

443 secondary formation of SO_4^{2-} and NO_3^-. The acid content in $PM_{2.5}$ was much higher at night under the promotion

444 of heterogeneous processes, resulting in stronger aerosol acidity and higher aerosol $\%Fe_S$. Furthermore,

445 photochemical reactions associated with oxalate likely played a considerable role in enhancing $\%Fe_S$ during

446 daylight hours, a trend more noticeable during the clean period. Oxalate might also be crucial in sustaining

447 elevated $\%Fe_S$ at night during the SP period.

448 This study provides insights into the mechanisms of aerosol $\%Fe_S$ modulation in the coastal city. The robust

449 promotion of aqueous-phase processes and the comparatively weaker influence of photochemistry on enhancing

450 aerosol $\%Fe_S$ were observed. In urban air, RH was a crucial factor in controlling $\%Fe_S$ through modulating the

451 heterogeneous reactions of SO_4^{2-} and NO_3^-. In contrast, in the oceanic atmospheric boundary layer, precursors'

levels and photochemical processes may be the decisive manipulators on aerosol %Fes. Therefore, the content of

bioavailable Fe in urban-related aerosols may be greatly elevated after intrusion into the marine atmosphere, which

holds significant importance for future research.

Author contributions. *WL: investigation, formal analysis, writing – original draft, writing – review and editing;*

YQ: methodology; YL: methodology; GW: visualization; YZ: methodology; JS: methodology; WQ: methodology;

LS: supervision, funding acquisition; WW: methodology; DZ: funding acquisition, methodology, writing – review

and editing; YZ: conceptualization, funding acquisition, methodology, supervision, writing – review and editing.

Acknowledgements. *We gratefully acknowledge the National Oceanic and Atmospheric Administration (NOAA)*

Air Resources Laboratory (ARL) for the provision of the HYSPLIT transport and dispersion model, available at

(https://www.ready.noaa.gov/HYSPLIT.php), and the Global Data Assimilation System (GDAS). Additionally, we

acknowledge the use of ISORROPIA II, accessible at (https://www.epfl.ch/labs/lapi/models-and-

software/isorropia/), developed by the Schools of Earth & Atmospheric Sciences and Chemical & Biomolecular

Engineering at the Georgia Institute of Technology, for the calculation of aerosol pH and liquid water content.

Competing interests. *The authors declare that they have no conflict of interests.*

Financial support. *This research was supported by National Natural Science Foundation of China (Grant Number:*

41875155, 41605114, 41875174) and the Overseas Joint Training Program for Doctoral Students of Ocean

University of China. D.Z. was supported by JSPS KAKENHI 21H01158.

References

Arimoto, R., Zhang, X. Y., Huebert, B. J., Kang, C. H., Savoie, D. L., Prospero, J. M., Sage, S. K., Schloesslin, C. A., Khaing, H. M., and Oh, S. N.: Chemical composition of atmospheric aerosols from Zhenbeitai, China, and Gosan, South Korea, during ACE-Asia, Journal of Geophysical Research: Atmospheres, 109, 10.1029/2003JD004323, 2004.

Baldo, C., Ito, A., Krom, M. D., Li, W., Jones, T., Drake, N., Ignatyev, K., Davidson, N., and Shi, Z.: Iron from coal combustion particles dissolves much faster than mineral dust under simulated atmospheric acidic conditions, Atmos. Chem. Phys., 22, 6045–6066, 10.5194/acp-22-6045-2022, 2022.

Chen, H. and Grassian, V. H.: Iron Dissolution of Dust Source Materials during Simulated Acidic Processing: The Effect of Sulfuric, Acetic, and Oxalic Acids, Environ. Sci. Technol., 47, 10312–10321, 10.1021/es401285s,

479   2013.

480   Chen, Y. and Siefert, R. L.: Seasonal and spatial distributions and dry deposition fluxes of atmospheric total and
481   labile iron over the tropical and subtropical North Atlantic Ocean, Journal of Geophysical Research:
482   Atmospheres, 109, https://doi.org/10.1029/2003JD003958, 2004.

483   Dou, J., Alpert, P. A., Corral Arroyo, P., Luo, B., Schneider, F., Xto, J., Huthwelker, T., Borca, C. N., Henzler, K.
484   D., Raabe, J., Watts, B., Herrmann, H., Peter, T., Ammann, M., and Krieger, U. K.: Photochemical degradation
485   of iron(III) citrate/citric acid aerosol quantified with the combination of three complementary experimental
486   techniques and a kinetic process model, Atmos. Chem. Phys., 21, 315–338, 10.5194/acp-21-315-2021, 2021.

487   Fu, H., Cwiertny, D. M., Carmichael, G. R., Scherer, M. M., and Grassian, V. H.: Photoreductive dissolution of
488   Fe-containing mineral dust particles in acidic media, Journal of Geophysical Research: Atmospheres, 115,
489   https://doi.org/10.1029/2009JD012702, 2010.

490   Fu, H., Lin, J., Shang, G., Dong, W., Grassian, V. H., Carmichael, G. R., Li, Y., and Chen, J.: Solubility of Iron
491   from Combustion Source Particles in Acidic Media Linked to Iron Speciation, Environ. Sci. Technol., 46,
492   11119–11127, 10.1021/es302558m, 2012.

493   Guo, H., Otjes, R., Schlag, P., Kiendler-Scharr, A., Nenes, A., and Weber, R. J.: Effectiveness of ammonia reduction
494   on control of fine particle nitrate, Atmos. Chem. Phys., 18, 12241–12256, 10.5194/acp-18-12241-2018, 2018.

495   Guo, H., Xu, L., Bougiatioti, A., Cerully, K. M., Capps, S. L., Hite Jr, J. R., Carlton, A. G., Lee, S. H., Bergin, M.
496   H., Ng, N. L., Nenes, A., and Weber, R. J.: Fine-particle water and pH in the southeastern United States,
497   Atmos. Chem. Phys., 15, 5211–5228, https://doi.org/10.5194/acp-15-5211-2015, 2015.

498   Hennigan, C. J., Izumi, J., Sullivan, A. P., Weber, R. J., and Nenes, A.: A critical evaluation of proxy methods used
499   to estimate the acidity of atmospheric particles, Atmos. Chem. Phys., 15, 2775–2790, 10.5194/acp-15-2775-
500   2015, 2015.

501   Hettiarachchi, E. and Rubasinghege, G.: Mechanistic Study on Iron Solubility in Atmospheric Mineral Dust
502   Aerosol: Roles of Titanium, Dissolved Oxygen, and Solar Flux in Solutions Containing Different Acid Anions,
503   ACS Earth and Space Chemistry, 4, 101–111, 10.1021/acsearthspacechem.9b00280, 2020.

504   Hettiarachchi, E., Hurab, O., and Rubasinghege, G.: Atmospheric Processing and Iron Mobilization of Ilmenite:
505   Iron-Containing Ternary Oxide in Mineral Dust Aerosol, The Journal of Physical Chemistry A, 122, 1291–
506   1302, 10.1021/acs.jpca.7b11320, 2018.

507   Hettiarachchi, E., Reynolds, R. L., Goldstein, H. L., Moskowitz, B., and Rubasinghege, G.: Bioavailable iron
508   production in airborne mineral dust: Controls by chemical composition and solar flux, Atmos. Environ., 205,
509   90–102, https://doi.org/10.1016/j.atmosenv.2019.02.037, 2019.

510   Hou, L., Dai, Q., Song, C., Liu, B., Guo, F., Dai, T., Li, L., Liu, B., Bi, X., Zhang, Y., and Feng, Y.: Revealing
511   Drivers of Haze Pollution by Explainable Machine Learning, Environmental Science & Technology Letters,
512   9, 112–119, 10.1021/acs.estlett.1c00865, 2022.

513   Huang, K., Zhuang, G., Li, J., Wang, Q., Sun, Y., Lin, Y., and Fu, J. S.: Mixing of Asian dust with pollution aerosol
514   and the transformation of aerosol components during the dust storm over China in spring 2007, Journal of
515   Geophysical Research: Atmospheres, 115, 10.1029/2009JD013145, 2010.

516   Li, J., Zhang, Y.-L., Cao, F., Zhang, W., Fan, M., Lee, X., and Michalski, G.: Stable Sulfur Isotopes Revealed a
517   Major Role of Transition-Metal Ion-Catalyzed SO_2 Oxidation in Haze Episodes, Environ. Sci. Technol., 54,
518   2626–2634, https://doi.org/10.1021/acs.est.9b07150, 2020.

519   Li, K., Fang, X., Wang, T., Gong, K., Ali Tahir, M., Wang, W., Han, J., Cheng, H., Xu, G., and Zhang, L.:
520   Atmospheric organic complexation enhanced sulfate formation and iron dissolution on nano α-Fe_2O_3,
521   Environmental Science: Nano, 8, 698–710, 10.1039/D0EN01220C, 2021.

Li, R., Zhang, H., Wang, F., He, Y., Huang, C., Luo, L., Dong, S., Jia, X., and Tang, M.: Mass fractions, solubility, speciation and isotopic compositions of iron in coal and municipal waste fly ash, Science of The Total Environment, 838, 155974, https://doi.org/10.1016/j.scitotenv.2022.155974, 2022.

Li, W., Qi, Y., Qu, W., Qu, W., Shi, J., Zhang, D., Liu, Y., Zhang, Y., Zhang, W., Ren, D., Ma, Y., Wang, X., Yi, L., Sheng, L., and Zhou, Y.: $PM_{2.5}$ source apportionment identified with total and soluble elements in positive matrix factorization, Sci. Total Environ., 858, 159948, https://doi.org/10.1016/j.scitotenv.2022.159948, 2023a.

Li, W., Qi, Y., Qu, W., Qu, W., Shi, J., Zhang, D., Liu, Y., Wu, F., Ma, Y., Zhang, Y., Ren, D., Du, X., Yang, S., Wang, X., Yi, L., Gao, X., Wang, W., Ma, Y., Sheng, L., and Zhou, Y.: Sulfate and nitrate elevation in reverse-transport dust plumes over coastal areas of China, Atmos. Environ., 295, 119518, https://doi.org/10.1016/j.atmosenv.2022.119518, 2023b.

Li, W., Xu, L., Liu, X., Zhang, J., Lin, Y., Yao, X., Gao, H., Zhang, D., Chen, J., Wang, W., Harrison, R. M., Zhang, X., Shao, L., Fu, P., Nenes, A., and Shi, Z.: Air pollution–aerosol interactions produce more bioavailable iron for ocean ecosystems, Sci. Adv., 3, e1601749, 10.1126/sciadv.1601749, 2017.

Liu, L., Lin, Q., Liang, Z., Du, R., Zhang, G., Zhu, Y., Qi, B., Zhou, S., and Li, W.: Variations in concentration and solubility of iron in atmospheric fine particles during the COVID-19 pandemic: An example from China, Gondwana Research, 97, 138–144, https://doi.org/10.1016/j.gr.2021.05.022, 2021a.

Liu, M., Song, Y., Zhou, T., Xu, Z., Yan, C., Zheng, M., Wu, Z., Hu, M., Wu, Y., and Zhu, T.: Fine particle pH during severe haze episodes in northern China, Geophys. Res. Lett., 44, 5213–5221, https://doi.org/10.1002/2017GL073210, 2017.

Liu, P., Ye, C., Xue, C., Zhang, C., Mu, Y., and Sun, X.: Formation mechanisms of atmospheric nitrate and sulfate during the winter haze pollution periods in Beijing: gas-phase, heterogeneous and aqueous-phase chemistry, Atmos. Chem. Phys., 20, 4153–4165, 10.5194/acp-20-4153-2020, 2020.

Liu, T., Chan, A. W. H., and Abbatt, J. P. D.: Multiphase Oxidation of Sulfur Dioxide in Aerosol Particles: Implications for Sulfate Formation in Polluted Environments, Environ. Sci. Technol., 55, 4227–4242, 10.1021/acs.est.0c06496, 2021b.

Lueder, U., Jørgensen, B. B., Kappler, A., and Schmidt, C.: Photochemistry of iron in aquatic environments, Environmental Science: Processes & Impacts, 22, 12–24, 10.1039/C9EM00415G, 2020.

Martin, J. H., Coale, K. H., Johnson, K. S., Fitzwater, S. E., Gordon, R. M., Tanner, S. J., Hunter, C. N., Elrod, V. A., Nowicki, J. L., Coley, T. L., Barber, R. T., Lindley, S., Watson, A. J., Van Scoy, K., Law, C. S., Liddicoat, M. I., Ling, R., Stanton, T., Stockel, J., Collins, C., Anderson, A., Bidigare, R., Ondrusek, M., Latasa, M., Millero, F. J., Lee, K., Yao, W., Zhang, J. Z., Friederich, G., Sakamoto, C., Chavez, F., Buck, K., Kolber, Z., Greene, R., Falkowski, P., Chisholm, S. W., Hoge, F., Swift, R., Yungel, J., Turner, S., Nightingale, P., Hatton, A., Liss, P., and Tindale, N. W.: Testing the iron hypothesis in ecosystems of the equatorial Pacific Ocean, Nature, 371, 123–129, 10.1038/371123a0, 1994.

Oakes, M., Ingall, E. D., Lai, B., Shafer, M. M., Hays, M. D., Liu, Z. G., Russell, A. G., and Weber, R. J.: Iron Solubility Related to Particle Sulfur Content in Source Emission and Ambient Fine Particles, Environ. Sci. Technol., 46, 6637–6644, 10.1021/es300701c, 2012.

Pang, H., Zhang, Q., Wang, H., Cai, D., Ma, Y., Li, L., Li, K., Lu, X., Chen, H., Yang, X., and Chen, J.: Photochemical Aging of Guaiacol by Fe(III)–Oxalate Complexes in Atmospheric Aqueous Phase, Environ. Sci. Technol., 53, 127–136, 10.1021/acs.est.8b04507, 2019.

Pye, H. O. T., Nenes, A., Alexander, B., Ault, A. P., Barth, M. C., Clegg, S. L., Collett Jr, J. L., Fahey, K. M., Hennigan, C. J., Herrmann, H., Kanakidou, M., Kelly, J. T., Ku, I. T., McNeill, V. F., Riemer, N., Schaefer,

T., Shi, G., Tilgner, A., Walker, J. T., Wang, T., Weber, R., Xing, J., Zaveri, R. A., and Zuend, A.: The acidity of atmospheric particles and clouds, Atmos. Chem. Phys., 20, 4809–4888, 10.5194/acp-20-4809-2020, 2020.

Sakata, K., Kurisu, M., Takeichi, Y., Sakaguchi, A., Tanimoto, H., Tamenori, Y., Matsuki, A., and Takahashi, Y.: Iron (Fe) speciation in size-fractionated aerosol particles in the Pacific Ocean: The role of organic complexation of Fe with humic-like substances in controlling Fe solubility, Atmos. Chem. Phys., 22, 9461–9482, 10.5194/acp-22-9461-2022, 2022.

Shi, J.-H., Zhang, J., Gao, H.-W., Tan, S.-C., Yao, X.-H., and Ren, J.-L.: Concentration, solubility and deposition flux of atmospheric particulate nutrients over the Yellow Sea, Deep Sea Research Part II: Topical Studies in Oceanography, 97, 43–50, https://doi.org/10.1016/j.dsr2.2013.05.004, 2013.

Shi, J., Guan, Y., Gao, H., Yao, X., Wang, R., and Zhang, D.: Aerosol Iron Solubility Specification in the Global Marine Atmosphere with Machine Learning, Environ. Sci. Technol., 56, 16453–16461, 10.1021/acs.est.2c05266, 2022.

Shi, J., Guan, Y., Ito, A., Gao, H., Yao, X., Baker, A. R., and Zhang, D.: High Production of Soluble Iron Promoted by Aerosol Acidification in Fog, Geophys. Res. Lett., 47, e2019GL086124, https://doi.org/10.1029/2019GL086124, 2020.

Shi, Z., Krom, M. D., Jickells, T. D., Bonneville, S., Carslaw, K. S., Mihalopoulos, N., Baker, A. R., and Benning, L. G.: Impacts on iron solubility in the mineral dust by processes in the source region and the atmosphere: A review, Aeolian Research, 5, 21–42, https://doi.org/10.1016/j.aeolia.2012.03.001, 2012.

Shi, Z. B., Krom, M. D., Bonneville, S., and Benning, L. G.: Atmospheric Processing Outside Clouds Increases Soluble Iron in Mineral Dust, Environ. Sci. Technol., 49, 1472–1477, 10.1021/es504623x, 2015.

Solmon, F., Chuang, P. Y., Meskhidze, N., and Chen, Y.: Acidic processing of mineral dust iron by anthropogenic compounds over the north Pacific Ocean, Journal of Geophysical Research: Atmospheres, 114, https://doi.org/10.1029/2008JD010417, 2009.

Song, S., Gao, M., Xu, W., Shao, J., Shi, G., Wang, S., Wang, Y., Sun, Y., and McElroy, M. B.: Fine-particle pH for Beijing winter haze as inferred from different thermodynamic equilibrium models, Atmos. Chem. Phys., 18, 7423–7438, 10.5194/acp-18-7423-2018, 2018.

Sorooshian, A., Wang, Z., Coggon, M. M., Jonsson, H. H., and Ervens, B.: Observations of Sharp Oxalate Reductions in Stratocumulus Clouds at Variable Altitudes: Organic Acid and Metal Measurements During the 2011 E-PEACE Campaign, Environ. Sci. Technol., 47, 7747–7756, 10.1021/es4012383, 2013.

Sugie, K., Nishioka, J., Kuma, K., Volkov, Y. N., and Nakatsuka, T.: Availability of particulate Fe to phytoplankton in the Sea of Okhotsk, Mar. Chem., 152, 20–31, https://doi.org/10.1016/j.marchem.2013.03.005, 2013.

Sun, P., Nie, W., Chi, X., Xie, Y., Huang, X., Xu, Z., Qi, X., Xu, Z., Wang, L., Wang, T., Zhang, Q., and Ding, A.: Two years of online measurement of fine particulate nitrate in the western Yangtze River Delta: influences of thermodynamics and N_2O_5 hydrolysis, Atmos. Chem. Phys., 18, 17177–17190, https://doi.org/10.5194/acp-18-17177-2018, 2018.

Tao, W., Su, H., Zheng, G., Wang, J., Wei, C., Liu, L., Ma, N., Li, M., Zhang, Q., Pöschl, U., and Cheng, Y.: Aerosol pH and chemical regimes of sulfate formation in aerosol water during winter haze in the North China Plain, Atmos. Chem. Phys., 20, 11729–11746, 10.5194/acp-20-11729-2020, 2020.

Tobo, Y., Zhang, D., Matsuki, A., and Iwasaka, Y.: Asian dust particles converted into aqueous droplets under remote marine atmospheric conditions, Proc. Natl. Acad. Sci. U.S.A., 107, 17905, 2010.

Toner, B. M.: An improved model of the ocean iron cycle, NATURE, 620, 41–42, https://doi.org/10.1038/d41586-023-02406-x, 2023.

Turpin, B. J. and Lim, H.-J.: Species Contributions to $PM_{2.5}$ Mass Concentrations: Revisiting Common

Assumptions for Estimating Organic Mass, Aerosol Science and Technology, 35, 602–610, 10.1080/02786820119445, 2001.

Wang, G., Tao, Y., Chen, J., Liu, C., Qin, X., Li, H., Yun, L., Zhang, M., Zheng, H., Gui, H., Liu, J., Huo, J., Fu, Q., Deng, C., and Huang, K.: Quantitative Decomposition of Influencing Factors to Aerosol pH Variation over the Coasts of the South China Sea, East China Sea, and Bohai Sea, Environmental Science & Technology Letters, 9, 815–821, https://doi.org/10.1021/acs.estlett.2c00527, 2022.

Wang, G., Zhang, R., Gomez, M. E., Yang, L., Zamora, M. L., Hu, M., Lin, Y., Peng, J., Guo, S., Meng, J., Li, J., Cheng, C., Hu, T., Ren, Y., Wang, Y., Gao, J., Cao, J., An, Z., Zhou, W., Li, G., Wang, J., Tian, P., Marrero-Ortiz, W., Secrest, J., Du, Z., Zheng, J., Shang, D., Zeng, L., Shao, M., Wang, W., Huang, Y., Wang, Y., Zhu, Y., Li, Y., Hu, J., Pan, B., Cai, L., Cheng, Y., Ji, Y., Zhang, F., Rosenfeld, D., Liss, P. S., Duce, R. A., Kolb, C. E., and Molina, M. J.: Persistent sulfate formation from London Fog to Chinese haze, Proc. Natl. Acad. Sci. U.S.A., 113, 13630, 2016.

Wang, H., Ding, J., Xu, J., Wen, J., Han, J., Wang, K., Shi, G., Feng, Y., Ivey, C. E., Wang, Y., Nenes, A., Zhao, Q., and Russell, A. G.: Aerosols in an arid environment: The role of aerosol water content, particulate acidity, precursors, and relative humidity on secondary inorganic aerosols, Science of The Total Environment, 646, 564–572, https://doi.org/10.1016/j.scitotenv.2018.07.321, 2019.

Wang, J., Zhao, B., Wang, S., Yang, F., Xing, J., Morawska, L., Ding, A., Kulmala, M., Kerminen, V.-M., Kujansuu, J., Wang, Z., Ding, D., Zhang, X., Wang, H., Tian, M., Petäjä, T., Jiang, J., and Hao, J.: Particulate matter pollution over China and the effects of control policies, Science of The Total Environment, 584–585, 426–447, https://doi.org/10.1016/j.scitotenv.2017.01.027, 2017.

Wang, Q., Zhuang, G., Li, J., Huang, K., Zhang, R., Jiang, Y., Lin, Y., and Fu, J. S.: Mixing of dust with pollution on the transport path of Asian dust - Revealed from the aerosol over Yulin, the north edge of Loess Plateau, Sci. Total Environ., 409, 573, 2011.

Wang, R., Balkanski, Y., Boucher, O., Bopp, L., Chappell, A., Ciais, P., Hauglustaine, D., Peñuelas, J., and Tao, S.: Sources, transport and deposition of iron in the global atmosphere, Atmos. Chem. Phys., 15, 6247–6270, 10.5194/acp-15-6247-2015, 2015.

Wang, X., Wei, W., Cheng, S., Zhang, H., and Yao, S.: Source estimation of SO_4^{2-} and NO_3^- based on monitoring-modeling approach during winter and summer seasons in Beijing and Tangshan, China, Atmos. Environ., 214, 116849, https://doi.org/10.1016/j.atmosenv.2019.116849, 2019.

Wang, Y., Hu, M., Hu, W., Zheng, J., Niu, H., Fang, X., Xu, N., Wu, Z., Guo, S., Wu, Y., Chen, W., Lu, S., Shao, M., Xie, S., Luo, B., and Zhang, Y.: Secondary Formation of Aerosols Under Typical High-Humidity Conditions in Wintertime Sichuan Basin, China: A Contrast to the North China Plain, J. Phys. Chem. A, 126, e2021JD034560, https://doi.org/10.1029/2021JD034560, 2021.

Watson, A. J. and Lefévre, N.: The sensitivity of atmospheric CO_2 concentrations to input of iron to the oceans, Tellus B: Chemical and Physical Meteorology, 51, 453–460, 10.3402/tellusb.v51i2.16320, 1999.

Watson, A. J., Law, C. S., Van Scoy, K. A., Millero, F. J., Yao, W., Friederich, G. E., Liddicoat, M. I., Wanninkhof, R. H., Barber, R. T., and Coale, K. H.: Minimal effect of iron fertilization on sea-surface carbon dioxide concentrations, Nature, 371, 143–145, 10.1038/371143a0, 1994.

Weller, C., Tilgner, A., Bräuer, P., and Herrmann, H.: Modeling the Impact of Iron–Carboxylate Photochemistry on Radical Budget and Carboxylate Degradation in Cloud Droplets and Particles, Environ. Sci. Technol., 48, 5652–5659, 10.1021/es4056643, 2014.

Wong, J. P. S., Yang, Y., Fang, T., Mulholland, J. A., Russell, A. G., Ebelt, S., Nenes, A., and Weber, R. J.: Fine Particle Iron in Soils and Road Dust Is Modulated by Coal-Fired Power Plant Sulfur, Environ. Sci. Technol.,

54, 7088–7096, 10.1021/acs.est.0c00483, 2020.

Wu, C. and Yu, J. Z.: Evaluation of linear regression techniques for atmospheric applications: the importance of appropriate weighting, Atmos. Meas. Tech., 11, 1233–1250, 10.5194/amt-11-1233-2018, 2018.

Wu, Y., Ge, X., Wang, J., Shen, Y., Ye, Z., Ge, S., Wu, Y., Yu, H., and Chen, M.: Responses of secondary aerosols to relative humidity and photochemical activities in an industrialized environment during late winter, Atmos. Environ., 193, 66–78, https://doi.org/10.1016/j.atmosenv.2018.09.008, 2018a.

Wu, Z., Wang, Y., Tan, T., Zhu, Y., Li, M., Shang, D., Wang, H., Lu, K., Guo, S., Zeng, L., and Zhang, Y.: Aerosol Liquid Water Driven by Anthropogenic Inorganic Salts: Implying Its Key Role in Haze Formation over the North China Plain, Environmental Science & Technology Letters, 5, 160–166, 10.1021/acs.estlett.8b00021, 2018b.

Xie, T., Lu, S., Zeng, J., Rao, L., Wang, X., Win, M. S., Zhang, D., Lu, H., Liu, X., and Wang, Q.: Soluble Fe release from iron-bearing clay mineral particles in acid environment and their oxidative potential, Science of The Total Environment, 726, 138650, https://doi.org/10.1016/j.scitotenv.2020.138650, 2020.

Xu, J., Chen, J., Zhao, N., Wang, G., Yu, G., Li, H., Huo, J., Lin, Y., Fu, Q., Guo, H., Deng, C., Lee, S. H., Chen, J., and Huang, K.: Importance of gas-particle partitioning of ammonia in haze formation in the rural agricultural environment, Atmos. Chem. Phys., 20, 7259–7269, 10.5194/acp-20-7259-2020, 2020.

Yang, T., Chen, Y., Zhou, S., Li, H., Wang, F., and Zhu, Y.: Solubilities and deposition fluxes of atmospheric Fe and Cu over the Northwest Pacific and its marginal seas, Atmos. Environ., 239, 117763, https://doi.org/10.1016/j.atmosenv.2020.117763, 2020.

Zhang, G., Lin, Q., Peng, L., Yang, Y., Jiang, F., Liu, F., Song, W., Chen, D., Cai, Z., Bi, X., Miller, M., Tang, M., Huang, W., Wang, X., Peng, P. a., and Sheng, G.: Oxalate Formation Enhanced by Fe-Containing Particles and Environmental Implications, Environ. Sci. Technol., 53, 1269–1277, 10.1021/acs.est.8b05280, 2019.

Zhang, H., Li, R., Dong, S., Wang, F., Zhu, Y., Meng, H., Huang, C., Ren, Y., Wang, X., Hu, X., Li, T., Peng, C., Zhang, G., Xue, L., Wang, X., and Tang, M.: Abundance and Fractional Solubility of Aerosol Iron During Winter at a Coastal City in Northern China: Similarities and Contrasts Between Fine and Coarse Particles, Journal of Geophysical Research: Atmospheres, 127, e2021JD036070, https://doi.org/10.1029/2021JD036070, 2022.

Zhang, Z., Boxall, C., and Kelsall, G. H.: Photoelectrophoresis of colloidal iron oxides 1. Hematite (α-Fe2O3), in: Colloids in the Aquatic Environment, edited by: Tadros, T. F., and Gregory, J., Elsevier, Oxford, 145–163, https://doi.org/10.1016/B978-1-85861-038-2.50014-0, 1993.

Zhou, M., Zhang, Y., Han, Y., Wu, J., Du, X., Xu, H., Feng, Y., and Han, S.: Spatial and temporal characteristics of $PM_{2.5}$ acidity during autumn in marine and coastal area of Bohai Sea, China, based on two-site contrast, Atmos. Res., 202, 196–204, https://doi.org/10.1016/j.atmosres.2017.11.014, 2018.

Zhou, Y., Zhang, Y., Griffith, S. M., Wu, G., Li, L., Zhao, Y., Li, M., Zhou, Z., and Yu, J. Z.: Field Evidence of Fe-Mediated Photochemical Degradation of Oxalate and Subsequent Sulfate Formation Observed by Single Particle Mass Spectrometry, Environ. Sci. Technol., 54, 6562–6574, 10.1021/acs.est.0c00443, 2020.

Zhu, X., Prospero, J. M., Savoie, D. L., Millero, F. J., Zika, R. G., and Saltzman, E. S.: Photoreduction of iron(III) in marine mineral aerosol solutions, Journal of Geophysical Research: Atmospheres, 98, 9039–9046, https://doi.org/10.1029/93JD00202, 1993.

Zhu, X. R., Prospero, J. M., and Millero, F. J.: Diel variability of soluble Fe(II) and soluble total Fe in North African dust in the trade winds at Barbados, Journal of Geophysical Research: Atmospheres, 102, 21297–21305, https://doi.org/10.1029/97JD01313, 1997.

Zhu, Y., Li, W., Lin, Q., Yuan, Q., Liu, L., Zhang, J., Zhang, Y., Shao, L., Niu, H., Yang, S., and Shi, Z.: Iron

694   solubility in fine particles associated with secondary acidic aerosols in east China, Environmental Pollution,
695   264, 114769, https://doi.org/10.1016/j.envpol.2020.114769, 2020.

696 Zhuang, G., Yi, Z., Duce, R. A., and Brown, P. R.: Link between iron and sulphur cycles suggested by detection
697   of Fe(n) in remote marine aerosols, Nature, 355, 537–539, 10.1038/355537a0, 1992.

698 Zuo, Y. and Hoigne, J.: Formation of hydrogen peroxide and depletion of oxalic acid in atmospheric water by
699   photolysis of iron(III)-oxalato complexes, Environ. Sci. Technol., 26, 1014–1022, 10.1021/es00029a022,
700   1992.
701